Chapter 5

Scaling analysis of anomalous Hall resistivity and magnetoresistance in magnetic shape memory Heusler compound: Mn_2NiGa

The present chapter involves a combined experimental and theoretical study of anomalous Hall data in the Mn_2NiGa compound, which concludes that the AHE due to the intrinsic Berry curvature is being suppressed as we move from the less symmetric tetragonal phase to the highly symmetric cubic phase, and suggesting that there is no straightforward rule to connect the Berry curvature to the mirror symmetry; rather, it depends on the symmetry-induced change in the electronic band structure. Additionally, we found that the large temperature dependence of AHE in the austenite cubic phase can be explained in terms of side jump mechanism.

5.1 Introduction

Shape memory alloys (SMAs) exhibit the temperature and/or stress-induced shape change due to structural phase transition from high temperature cubic (austenite) to low temperature tetragonal (martensite) phase upon cooling and have the capability to revert to its predetermined shape upon heating [1, 2, 3, 4]. These alloys have diverse technological applications ranging from ground, marine and aerospace structures to biomedical implants, energy conversion devices, actuators and smart structures, to name just a few [5, 6, 7]. Magnetic shape memory alloys (MSMAs) are particular SMAs, which produces much larger deformation/strain not only under the influence of temperature and stress but also on the application of magnetic field in the low temperature martensite phase and offers advantage over the conventional SMAs [8, 9, 10, 11, 12, 13, 14].

MSMAs may provide a perfect platform to better understand the correlation between crystal symmetry and electronic transport properties of materials. A recent study on Ni_2MnGa magnetic shape memory (MSM) Heusler compound indicates a large intrinsic anomalous Hall conductivity (IAHC) $\sim$57.9 S/cm in low-temperature tetragonal phase as compared to the IAHC of $\sim$21.5 S/cm in the high-temperature cubic phase [17]. This study indicates the intrinsic mechanism is getting suppressed when moving toward the highly symmetric cubic crystal system. However, several studies show that greater symmetry results in larger Berry curvature, which is responsible for higher IAHC [15, 16], and the contradictory result in Ni_2MnGa MSM Heusler compound motivates for further studies in the similar MSM Heusler compounds. The Mn_2NiGa MSM Heusler compound in which the anomalous Hall effect has previously been observed, making it a promising platform to explore

and extend our understanding of the change in IAHC associated with structural phase transition.

Here, we report different aspects of the scattering mechanism in the Mn_2NiGa MSM Heusler compound by analyzing the resistivity, magnetoresistance, and Hall data. In the low-temperature martensite region, the scaling behavior of anomalous Hall resistivity (AHR) reflects that the extrinsic skew scattering mechanism has a nearly equal contribution to the AHE as the intrinsic mechanism. The obtained value of experimental IAHC is $\sim$12 S/cm, which is very less as compared to the theoretical value $\sim$131 S/cm, which could be due to the formation of twin domain in the low-temperature martensite phase. Whereas, in the high-temperature austenite region, the scaling behavior of AHR reflects that the extrinsic skew scattering and side jump mechanisms in the dominate over the intrinsic mechanism. Both the quadratic dependency of longitudinal resistivity on temperature and the linear negative magnetoresistance confirm the dominance of electron-magnon coupling in the Mn_2NiGa compound. The detailed analysis asserts the side jump mechanism plays a crucial role in the austenite phase because of the electron-magnon coupling present in the Mn_2NiGa compound. The experiment indicates that the intrinsic mechanism is being suppressed when moving toward the highly symmetric cubic crystal system. The theoretical value of IAHC in the low-temperature martensite phase is calculated to be $\sim$131 S/cm, larger than the theoretical value of $\sim$75 S/cm in the high-temperature austenite phase, which is in good agreement with the experimental finding that as moving toward the highly symmetric cubic phase the intrinsic mechanism is getting suppressed.

5.2 Methods

The polycrystalline Mn_2NiGa ternary compound is prepared by the standard arc-melting method [18, 19]. The details of the sample preparation method and the data collection have already been reported elsewhere [20].

The theoretical studies are performed with the help of widely used QUANTUM ESPRESSO (QE) simulation package [21]. QE is one of the planewave methods which works within the framework of pseudopotentials (PPs). To account for the exchange and correlation potential of the DFT Hamiltonian, norm-conserving GGA [22] functionals are used through ONCV PPs [23] for which the planewave kinetic energy cutoff is taken as 80 Ry. The Gaussian smearing of 0.01 Ry is used both

for the self-consistent (SC) and non-self-consistent (NSC) calculations. The threshold for the SC total energy calculations has been set to 10^{-8} Ry. WANNIER90 package (implemented within QE) is used for projecting the Bloch wave functions into maximally localized Wannier functions to compute the Berry curvature and thereby the IAHC [21, 24, 25, 26]. Spin-orbit coupling (SOC) is introduced in all the Berry curvature-related calculations. The same **k**-grid of $8 \times 8 \times 8$ is taken everywhere, SC, NSC, and WANNIER90 calculations. The transition-metal d orbitals (as the projections) are found to provide very good matching of WANNIER bands with the full DFT bands. A dense **k**-mesh of $75 \times 75 \times 75$ is considered in the anomalous Hall conductivity (AHC) calculation. The **k**-mesh was made further denser, by adding a refined mesh of $5 \times 5 \times 5$ through adaptive refinement technique around the points wherever the mode of the Berry curvature exceeds 100 bohr^2.

5.3 Results and discussion

5.3.1 Anomalous Hall effect

Temperature-dependent magnetization data in cooling cycle, which is reported in our recent study on the Mn_2NiGa compound [20], indicates that the austenite to martensite phase transition starts at a temperature around 284 K. The Hall measurement was performed at different temperatures (in the temperature range of 360-5 K) in cooling sequence. The sharp increase of isothermal Hall resistivity (ρ_{xy}) in low magnetic field region, unveils the presence of anomalous Hall resistivity. In the high magnetic field region, ρ_{xy} is described by the following relation [27, 28]-

$$\rho_{xy} = R_0 H + R_s M_s \tag{5.1}$$

where R_0, R_s, and M_s are the ordinary Hall coefficient, anomalous Hall coefficient, and saturation magnetization (reported in literature [20]), respectively. $R_s M_s$ represents the anomalous Hall resistivity (ρ_{AH}). ρ_{xy} increases steeply up to field 1 T due to the presence of ρ_{AH}. In the higher field region (>1 T), ρ_{xy} changes linearly and shows a slope with the magnetic field, which is due to the ordinary Hall effect [29]. To separate out the ordinary and anomalous Hall contributions, we performed fitting of the ρ_{xy} versus H data by using the above equation in the higher field region (>2

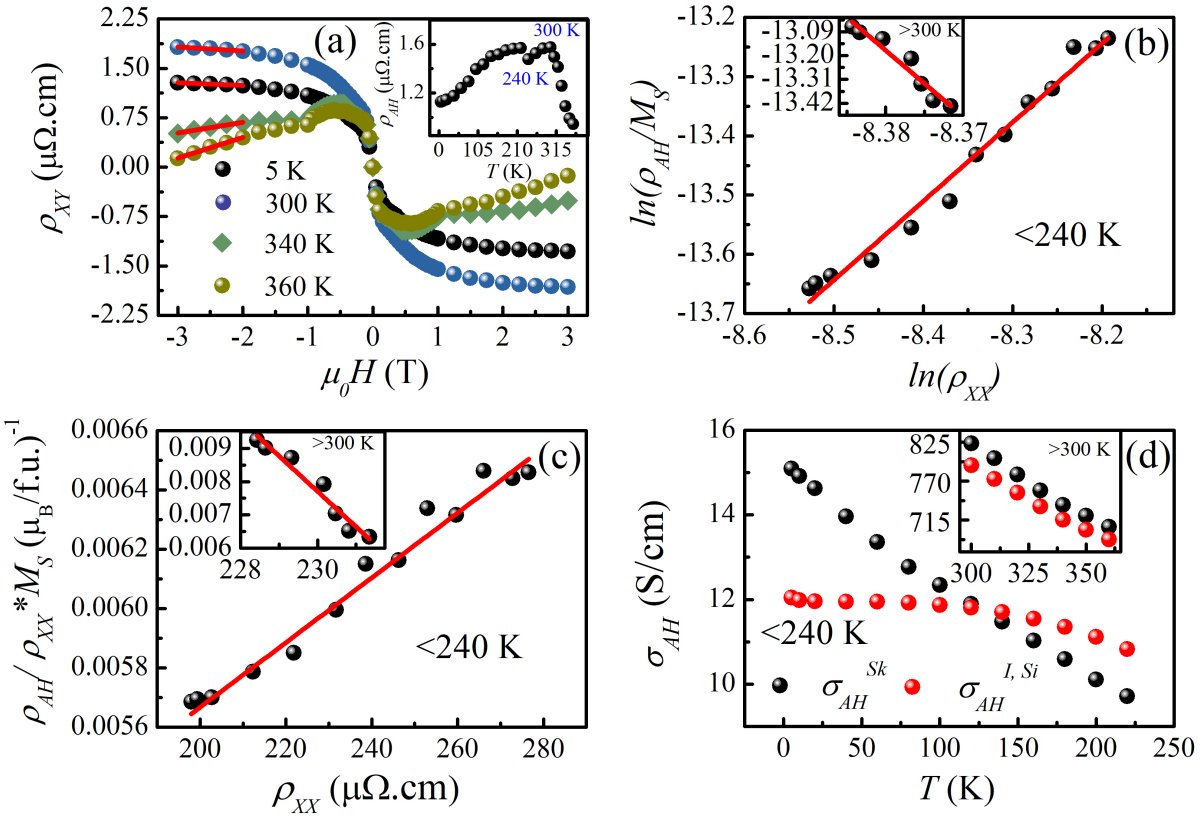

Figure 5.1: (a) The high field linear fitting of the field-dependent Hall resistivity curves at different temperatures. Inset shows the temperature-dependent anomalous Hall resistivity. (b) Linear fitting of log(ρ_{AH}) vs log(ρ_{XX}) data in the low-temperature martensite phase. Inset of (b) shows the linear fitting of the same data in the high-temperature austenite phase. (c) Fitting of the ratio of anomalous Hall resistivity and longitudinal resistivity ρ_{AH}/ρ_{XX}) vs ρ_{XX} data in the low-temperature martensite phase. Inset of (c) shows the same fitting in the high-temperature austenite phase. (d) Different contributions of σ_{AH} with temperature are plotted on the same scale in the low-temperature martensite phase. Inset of (d) shows the same plot in the high-temperature austenite phase.

T), as shown in Fig. 5.1(a). The fitting of the ρ_{xy} versus H at different temperatures provides the value of R_0 and R_sM_s that correspond to the slope and intercept of the fitted line. The temperature-dependent ρ_{AH} [inset of Fig. 5.1(a)], which is the intercept R_sM_s, indicates the larger variation in ρ_{AH} with the temperature above 300 K as compared to the temperature region below 240 K. This observation is related to the thermally activated martensite transition from high-temperature cubic to low-temperature tetragonal phase, which is a well-established phenomenon in the Mn_2NiGa MSM Heusler compound [20, 30].

In the low-temperature martensite phase (5 K<T<240 K), the negative sign of R_0 [Fig. 5.2] reflects that electrons are the dominating charge carrier in transport. Whereas, in the high-temperature austenite phase (300 K<T<360 K), the positive sign of R_0 [Fig. 5.2] reflects that holes are the dom-

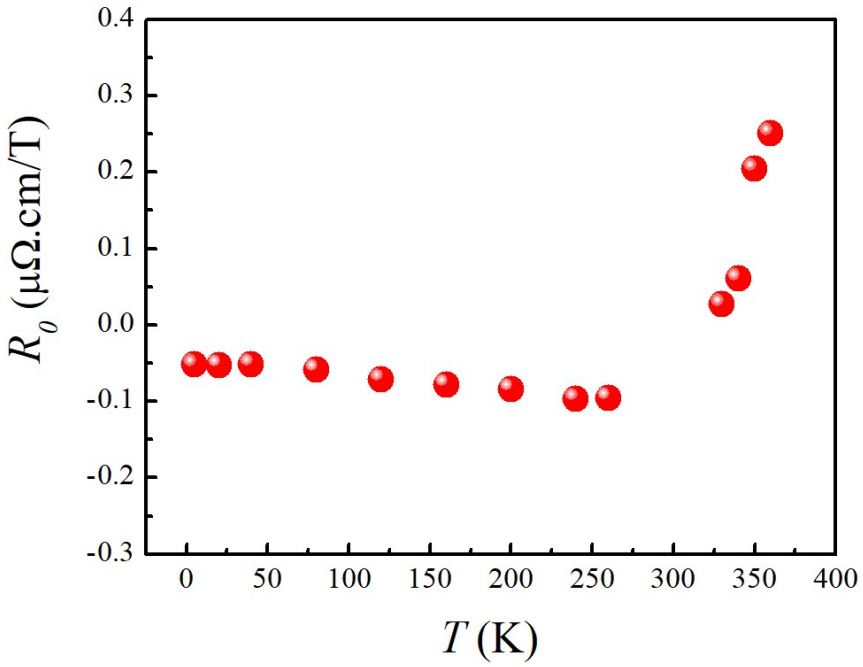

Figure 5.2: Variation of the ordinary Hall coefficient (R_0) as a function of temperature.

inating charge carrier in transport. The carrier concentration (n) determined by the expression $n = \frac{1}{eR_0}$, was found to be $\sim 4\times10^{20}$cm^{-3} and $\sim 1\times10^{20}$cm^{-3} at 5 K and 360 K, respectively, which is comparable with the literature on Mn_2 based Heusler system [31].

The dominating mechanism in the AHE can be evaluated by the exponent β using the scaling relation $\rho_{AH} \propto \rho_{xx}{}^{\beta}$ [29, 32, 35]. If $\beta = 1$, the skew scattering mechanism will be dominant in AHE, and if $\beta = 2$, the combination of side jump and intrinsic mechanism will largely contribute to the AHE. In the low-temperature martensite phase, the exponent β determined by linear fitting of $\ln(\rho_{AH})$ versus $\ln(\rho_{xx})$ as shown in Fig. 5.1(b) is turned out to be $\sim$1.33, which reflects that not only intrinsic and side jump mechanisms but skew scattering mechanism is also contributing to AHE [33]. In the high-temperature austenite phase, the value of exponent β is found to be $\sim 30 >> 2$, which shows that the extrinsic mechanism (skew scattering + side jump) is largely contributing to AHE as compared to the intrinsic mechanism [34].

To calculate the separate contributions of extrinsic and intrinsic mechanisms in the total AHE, the $\frac{\rho_{AH}}{\rho_{xx} M_S}$ versus ρ_{xx} data (black dots in Fig. 5.1(c)) was fitted (red line in Fig. 5.1(c)) using the following relation [36]-

$$\rho_{AH} = a(M_s)\rho_{xx} + b(M_s){\rho_{xx}}^2 \tag{5.2}$$

where the linearly magnetization dependent parameters *a(M_s)* and *b(M_s)* contain information about extrinsic skew scattering and the combined effect of extrinsic side jump and intrinsic contribution, respectively. M_s is the saturation magnetization at different temperatures, obtained from field-dependent magnetization data reported in our recent study on the Mn_2NiGa compound [20]. In the low-temperature martensite phase, the fitting gives the value of coefficients a(Ms) and b(Ms) as 0.0033 and 12 S/cm at 5 K, respectively. Whereas, in the high-temperature austenite phase, the fitting as shown in the inset of Fig. 5.1(c) gives the value of coefficients a(Ms) and b(Ms) is 0.1881 and -793 S/cm at 300 K, respectively. The negative sign of b(Ms) represents the combined side jump, and the intrinsic contribution is opposite to the skew scattering contribution.

By using the obtained value of coefficients a(Ms) and b(Ms), we calculated the separate contribution in AHC (σ_{AH}) due to the skew scattering and the combined side jump and intrinsic mechanisms. Fig. 5.1(d) shows the variation of AHC due to the skew scattering mechanism (σ_{AH}^{Sk}) and the combined side jump and intrinsic mechanism ($\sigma_{AH}^{I,Si}$) with temperature. In the low-temperature martensite phase, we may clearly see that σ_{AH}^{Sk} is linearly dependent on temperature as expected and $\sigma_{AH}^{I,Si}$ is nearly independent of temperature. It is a well-established fact that the side jump contribution is independent of both scattering strength and disorder density and it can be neglected for ferromagnetic metals [29, 33]. Therefore, in the martensite phase, the skew scattering mechanism is more or less equally responsible for AHE as the intrinsic mechanism, and the value of IAHC (σ_{AH}^{I}) = b(Ms) = 12 S/cm. Whereas, in high-temperature region σ_{AH}^{Sk} is showing the same behavior but $\sigma_{AH}^{I,Si}$ reflects significant dependency on temperature, which may be related to the dominance of side jump as compared to the intrinsic mechanism.

It has been theoretically discovered that side jump has a strong dependence upon the spin structure of the scattering potential [37]. This result indicates that electron-magnon scattering plays a crucial role in AHE, along with normal impurity scattering and phonon scattering. Experimental studies also suggest the electron-magnon scattering induced side jump contribution [38, 39]. To confirm the presence of electron-magnon scattering, we have analyzed the temperature and magnetic field-

dependent longitudinal resistivity data that is reported in the literature [20].

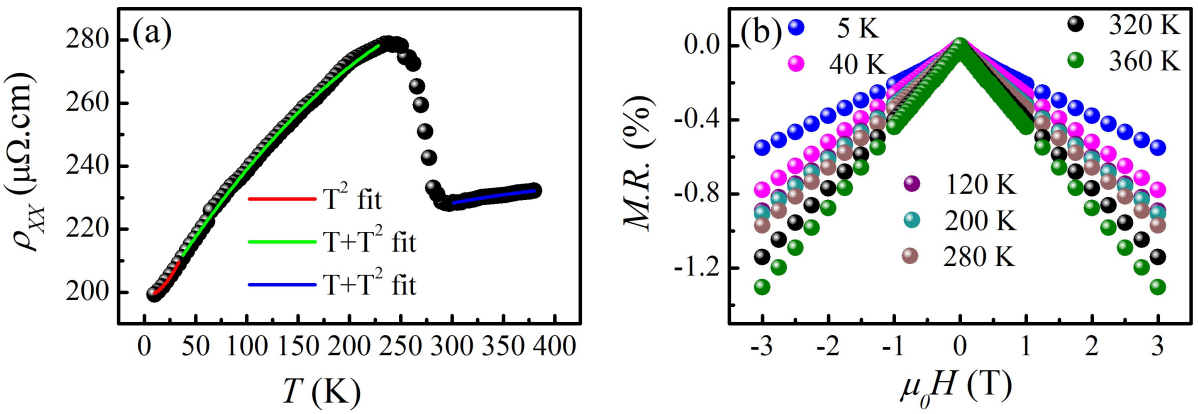

Figure 5.3: (a) The longitudinal resistivity (ρ_{xx}) versus temperature (T) data (black dots) in cooling sequence. The continuous red, green, and blue lines are fitted curves in different temperature regions. (b) The plot of magneto-resistance (M.R.) at different temperatures.

The reported temperature-dependent longitudinal resistivity data [20] shows the resistivity decreases with the decrease in temperature with an abrupt increase in resistivity around 300 K, showing the metallic behavior of the Mn_2NiGa system. It is found that the residual resistivity is $\sim$200 $\mu\Omega$.cm, which is well matching with the literature [19]. Generally, the presence of disorder in a metal is speculated by its residual resistivity ratio (RRR), i.e., the ratio of the resistivities at 300 and 5 K. For the Mn_2NiGa system, RRR is $\sim$1.4, comparable to the literature and indicating that we can not neglect the possibility of disorder [19].

Usually, the resistivity arises from the different scattering mechanisms. To probe the microscopic mechanisms responsible for the distinct nature of ρ_{xx}-T data, we divided our analysis into the specific temperature ranges 5-35 K, 35-240 K, and 300-360 K. In the high-temperature region (300 K$<$T$<$380 K), the resistivity data follows a sum of linear and quadratic dependence with temperature ($\rho \propto T+T^2$), which is reflected by the blue continuous line in Fig. 5.3(a). As the temperature decreases, i.e., in the range (240 K$>$T$>$35 K), the resistivity data follows the same behavior as in the high-temperature range, which is shown by the green continuous line in Fig. 5.3(a). This is ascribed to the presence of electron-phonon scattering ($\rho \propto T$) [40] along with electron-magnon scattering ($\rho \propto T^2$) [41]. In the low-temperature region (35 K$>$T$>$5 K), the resistivity shows pure quadratic behavior with temperature, which is shown by the red continuous line in Fig. 5.3(a). The behavior reflects the dominance of the electron-magnon scattering mechanism.

By using the reported magnetic field-dependent ρ_{xx} data [20], we have calculated the isothermal magnetoresistance (M.R.) in the temperature range 5-360 K [Fig. 5.3(b)]. The M.R. is calculated using the following relation [42]-

$$M.R. = \frac{\rho_{xx}(H) - \rho_{xx}(0)}{\rho_{xx}(0)} \tag{5.3}$$

where ρ_{xx}(H) and ρ_{xx}(0) are longitudinal resistivities at a particular field H and at zero field, respectively. The longitudinal resistivity decreases with the application of the magnetic field, which results in negative M.R. This behavior is ascribed to the damped spin wave excitation with the increase in the magnetic field, which leads to the suppression in the electron-magnon coupling. Theory suggests that the negative M.R. due to the electron-magnon scattering can be described by the following equation, which is valid for fields below 100 T and for the temperature range of $T_c/5$ to $T_c/2$ [43].

$$\Delta\rho_{xx}(T,H) \propto \frac{HT}{D(T)^2} ln \frac{\mu_B H}{k_B T} \tag{5.4}$$

where *D(T)* is the magnon stiffness or the magnon mass renormalization. The first-order approximation of magnon stiffness is described as $D(T) \sim D_0(1\text{-}d_1T^2)$ where D_0 is the zero temperature magnon mass, and d_1 is a constant [44]. Fig. 5.4(a) shows that the field-dependent longitudinal resistivity fits well with the above equation, and this confirms that the linear M.R. is found because of the suppression in electron-magnon scattering. Therefore, both the quadratic temperature dependency of resistivity and linear negative M.R. suggest the dominance of electron-magnon coupling in the Mn_2NiGa system.

Furthermore, it is obvious from Fig. 5.3(b) that negative M.R. decreases with the decrease in temperature because the spin-flip transition reduces at low temperatures and this leads to the declination in the magnon population. Hence, the electron-magnon coupling is higher in the high-temperature region as compared to the low-temperature region. The slope of high-field M.R. is significantly dependent on the temperature and can be described by the following equation [43, 44]-

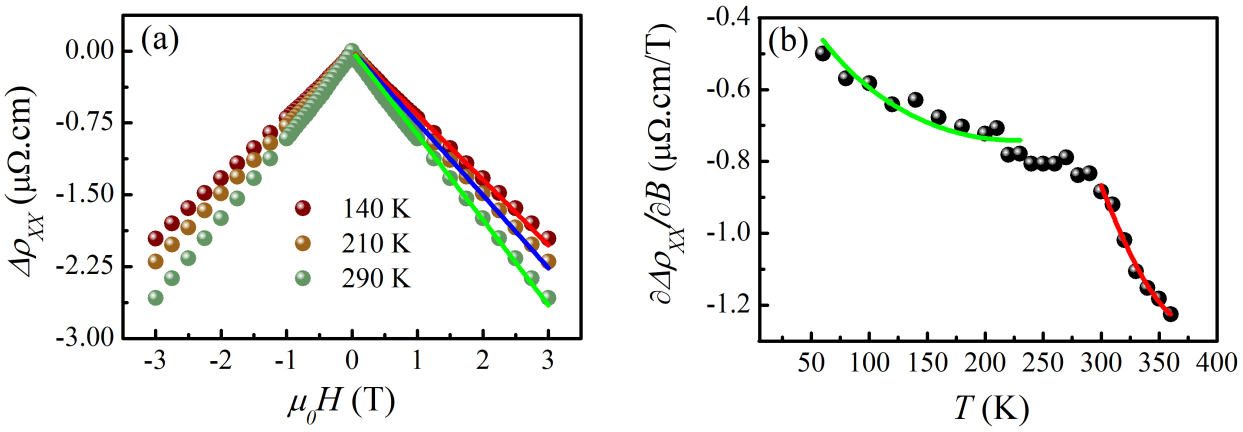

Figure 5.4: (a) The field-dependent change in longitudinal resistivity at different temperatures and the continuous lines are fit to Eq. (3.4). (b) The variation of $\frac{\delta\Delta\rho_{xx}}{\delta H}$ with temperature. The continuous lines are fit using Eq. (3.5).

$$\frac{\delta\Delta\rho_{xx}}{\delta H} \propto T(1+2d_1T^2)[ln(T)+C_{te}] \tag{5.5}$$

where d_1 is a constant that depends on the zero-temperature magnon mass and c_{te} is a temperature-independent term. It is observed that the temperature-dependent slope of high-field M.R. as shown in Fig. 5.4(b) changes its nature in specific temperature ranges 5-240 K and 300-360 K. In the low-temperature range (5 <T<240 K), the above equation provides a good fit for the data with d_1 = 10^{-6} K^{-2}. Whereas, in the high-temperature range (300 K<T<360 K), the obtained value of d_1 = 10^{-5} K^{-2}, which is 10 times larger than the low-temperature region. The large value of d_1 depicts a stronger temperature dependence of magnon stiffness in the high-temperature austenite phase.

Fig. 5.5(a) shows that in the martensite phase, σ_{AH} is showing linear temperature dependence as longitudinal conductivity σ_{xx} = $1/\rho_{xx}$ but the slope of σ_{AH} is slightly lower than σ_{xx} because of the appreciable contribution of intrinsic mechanism to σ_{AH}. On the other hand, in the austenite phase, σ_{AH} largely varies with temperature as compared to σ_{xx} due to the dominant contribution of side jump in addition to skew scattering. In order to confirm the role of magnons and their influence on the temperature dependence of the side jump mechanism, the temperature dependence change in resistivity under field, i.e., $\Delta\rho_{xx}^{3T}$ is plotted with $\rho_{AH}^{I,Sj}$. Fig. 5.5 (b) indicates that $\rho_{AH}^{I,Sj}$ is linearly varying with $\Delta\rho_{xx}^{3T}$ supported by the linear fitting, which elucidates that in high-temperature austenite phase the temperature dependence of $\rho_{AH}^{I,Sj}$ is originated from the electron-magnon scattering. Our

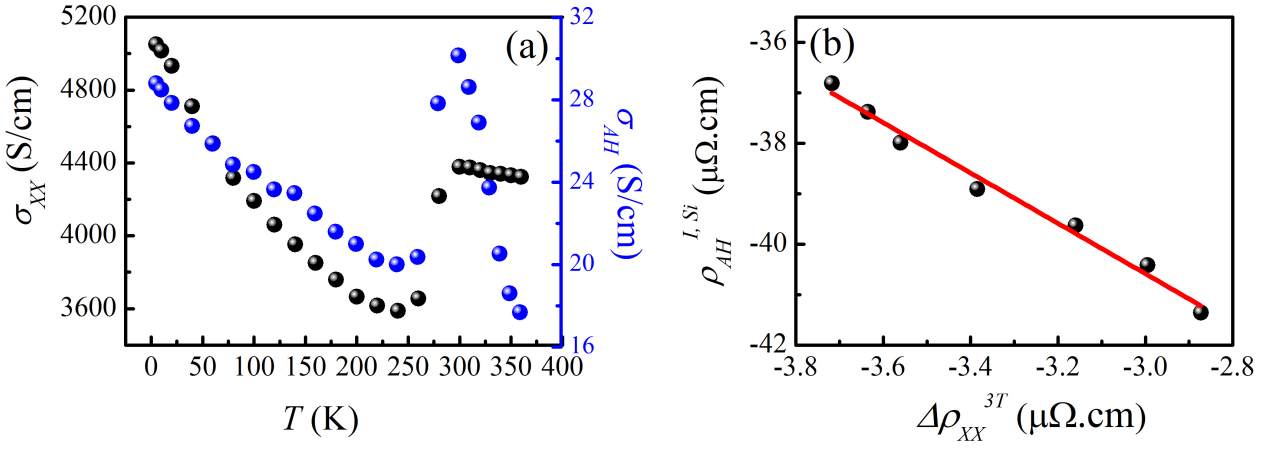

Figure 5.5: (a) Temperature-dependent longitudinal conductivity σ_{xx} (black spheres) and AHC (blue spheres). (b) The linear fit between the combined side jump and intrinsic contribution to anomalous Hall resistivity $\rho_{AH}^{I,Sj}$ and change in resistivity with field ($\Delta\rho_{xx}^{3T}$).

results conclude that despite the dominance of the intrinsic contribution to AHE connected with the topological band structure, the temperature dependence of AHE can be explained by the electron-magnon scattering mechanism. Thus, the experimental findings suggest that the intrinsic mechanism is being suppressed as we move toward the highly symmetric cubic phase in the high-temperature region above room temperature.

5.3.2 First-principle calculations

Now, to investigate the effect of structural change on the transport property and correlate it with the experimental results, we have further performed theoretical calculations. In our earlier work [31], excellent agreement between the measured and calculated AHC has been found. We believe that an approach of projecting the Bloch wave functions into maximally localized Wannier functions works pretty well in predicting AHC for systems in which the AHE is governed by a Berry curvature-driven intrinsic mechanism. However, as we discussed, the AHC in the martensite Mn_2NiGa has an around equal contribution by extrinsic skew scattering as intrinsic mechanisms. The extrinsic skew and side jump contribution is enhanced in the austenite phase. Thus, the experimental results clearly conclude that the intrinsic mechanism controls the AHC in the martensite phase to a greater extent than in the austenite phase. In the present case also, we carry out DFT calculations to compare the theoretical values with the observed ones.

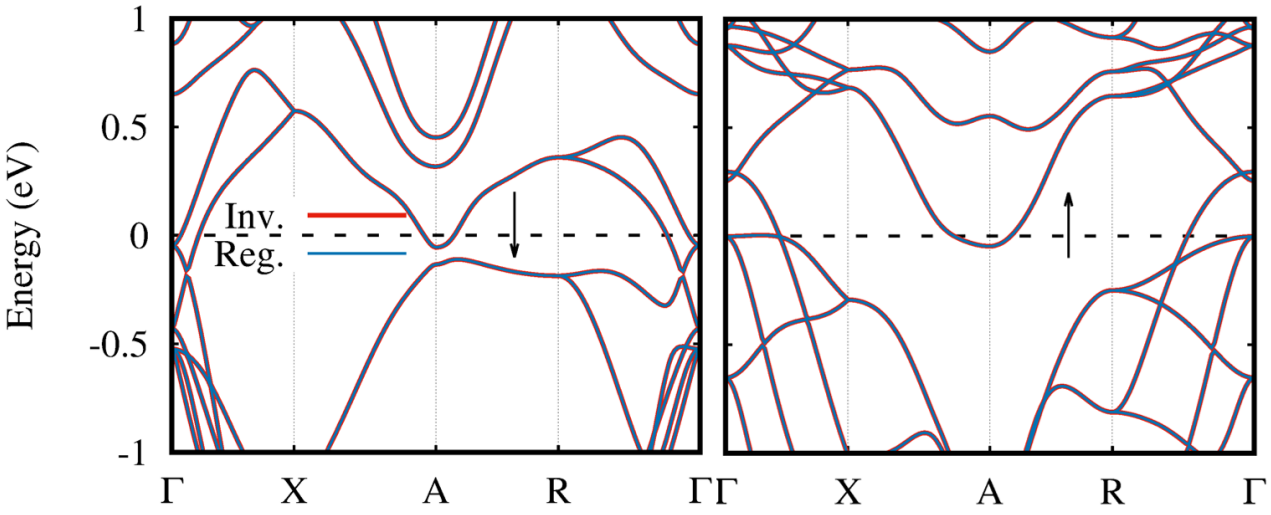

Figure 5.6: Spin-minority (left) and majority (right) band structures of martensite Mn_2NiGa are compared for the regular and inverse tetragonal structures. The Fermi energy is set to 0 eV. As we can see, the band structures are exactly the same for both cases. Hence, all the physical quantities that can be extracted from the electronic bands are expected to be the same in both cases.

We first consider the martensite phase of regular tetragonal structure (I4/mmm) in the theoretical calculations. The local magnetic moment is found to be -2.6 μ_B and 3.2 μ_B for Mn at 2d and 2b sites, respectively, which is well matched with the literature [45]. As expected in the literature, the martensite phase can also crystallize in an inverse tetragonal structure ($I\bar{4}m2$); we have also calculated the local magnetic moment for this structure, giving the same result as the regular one. For both the cases (regular and inverse), we have obtained very good WANNIER interpolation before calculating the IAHC in the Berry curvature approach [26, 46]. The obtained IAHCs for the regular and inverse tetragonal structures are 132 S/cm and 125 S/cm, respectively,. The similar magnitudes in both cases are attributed to their almost same electronic band features (Fig. 5.6) because the intrinsic contribution to the AHC purely depends on the band structure. However, the calculated AHC in the tetragonal martensite phases is not comparable with the experimental values. The formation of microstructures (not captured in theory) in the tetragonal phase might lead to a mismatch between theoretical and experimental AHCs.

There is the possibility that the anti-site disorder, already established in this system, is playing a role in deciding the experimental IAHC. So, we have calculated IAHC by incorporating 50% antisite disorder between Mn (4d site) and Ga (2b site) within the regular tetragonal structure. We compared the full DFT band structure of disordered Mn_2NiGa with the Wannier interpolated one in Fig. 5.7

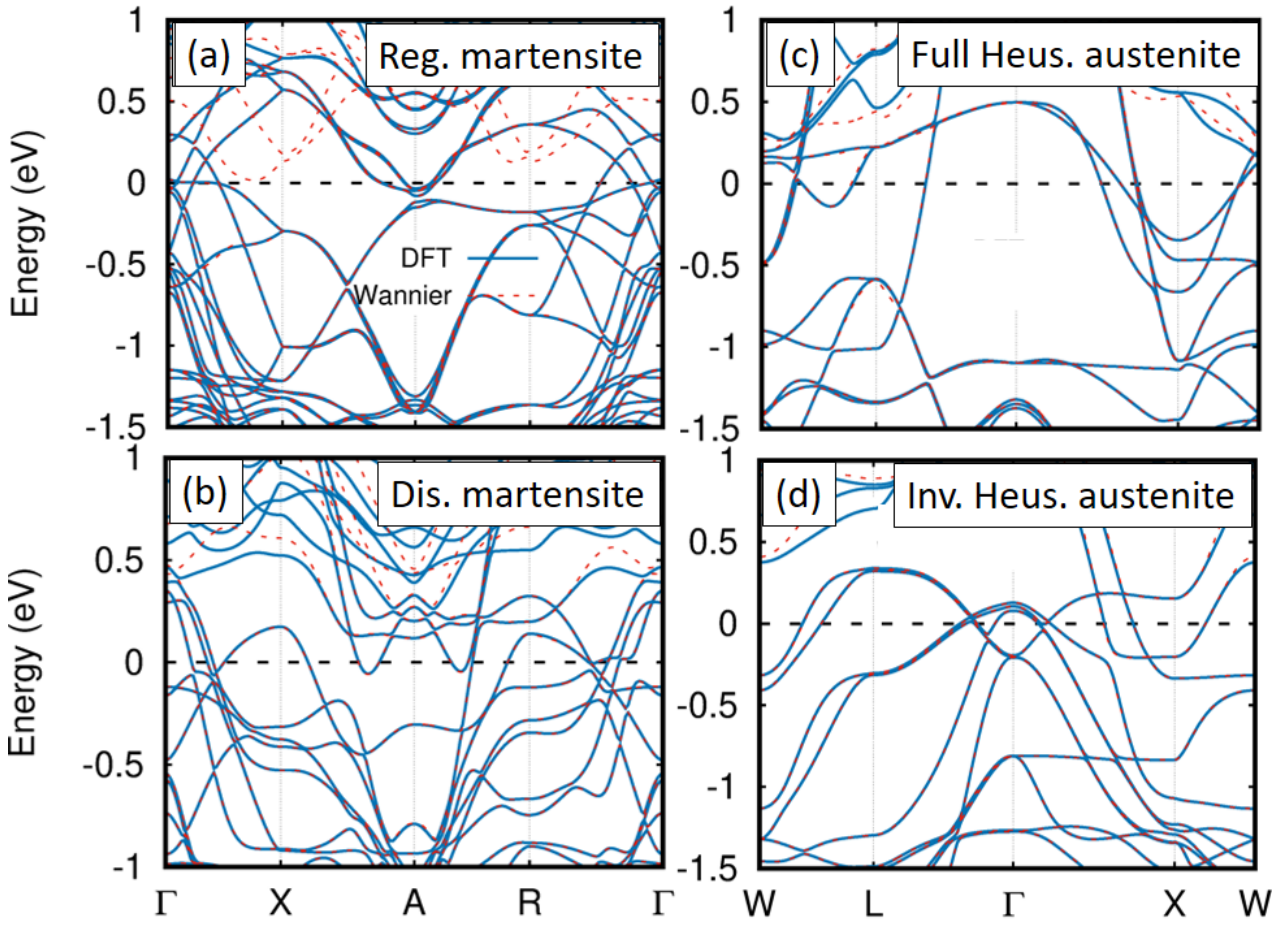

Figure 5.7: (a), (b), (c), and (d) Full electronic band structure (blue continuous line) and Wannier interpolated band structure (red dashed line) of ordered tetragonal, disordered tetragonal, $Fm\bar{3}m$ cubic and $F\bar{4}3m$ cubic Mn_2NiGa respectively. The Fermi energy is set to 0 eV.

(b) and obtained a very good interpolation. The calculated value of IAHC is ∼792 S/cm, indicating that anti-site disorder enhances the IAHC. Hence, the reason behind getting small IAHC (12 S/cm) by experiment may not be related to the anti-site disorder; it might be related to the formation of the twin domains and modulation in the regular tetragonal martensite phase [47, 48]. The theory is not able to consider these types of twin domain formation and modulation in its calculation.

Experimentally, we have observed different mechanisms govern the AHC in different phases of Mn_2NiGa. Therefore, in addition to the martensite phase, we calculate the AHC in the cubic austenite phase to compare with the experimental results. In this regard, we have considered two possible cubic crystal structures of the Mn_2NiGa; regular full Heusler (space group $Fm\bar{3}m$) and inverse Heusler ($F\bar{4}3m$) for the AHC calculation. The calculated AHC in the $Fm\bar{3}m$ case is ∼75 S/cm. $F\bar{4}3m$ structure provides sufficiently low AHC (∼10 S/cm). In the latter case, the absence of any

avoided band crossing or near degeneracy at the Fermi energy results in extremely low AHC. A similar magnitude is also reported by us in Mn_2CoAl spin gapless semiconductor, an inverse Heusler compound [31]. Thus, we may conclude that the theoretical IAHC due to momentum space Berry curvature in the low-temperature martensite phase is higher than in the high-temperature austenite phase. Similarly, experimental analysis shows that the momentum space Berry curvature raises the AHC in the low-temperature martensite phase to a greater extent than in the high-temperature austenite phase.

The comparative study for martensite tetragonal and austenite cubic phase suggest that the intrinsic mechanism is getting suppressed in the highly symmetric cubic phase (9 mirror planes) compared to the low symmetric tetragonal phase (5 mirror planes). Several theoretical and experimental studies on Fe_2- and Co_2-based Heusler systems [15, 16] show that greater mirror plane symmetry results in larger Berry curvature, which is responsible for the higher IAHC. Therefore, our combined experimental and theoretical results suggest that there is no elementary rule to connect the Berry curvature to the mirror symmetry, but rather it depends on the symmetry-induced change in the electronic band structure, which is different for different crystal systems. Our result is in good agreement with the previous result found for the Co_2FeAl system [49]. If the crystal symmetry is such that it brings the band crossings or avoided band crossing very close to the Fermi energy, then the value of IAHC due to Berry curvature will be large. Hence, our results provide a platform for the systematic investigation of AHE in MSM Heusler and related systems.

5.4 Conclusion

In summary, a detailed scaling analysis reveals that in the high-temperature cubic phase the AHE is mainly driven by extrinsic skew scattering and side jump mechanisms. The analysis of temperature-dependent resistivity and magnetoresistance reflects that electron magnon scattering dominates the change in resistivity as a function of temperature in the high-temperature cubic phase of the Mn_2NiGa compound. On the other hand, temperature-dependent magnetoresistance at high fields is correlated with the side jump contribution in AHE. This validates that the side jump contribution originates from the electron magnon scattering. Whereas, in the low-temperature martensite phase, the skew

scattering mechanism has a nearly equal contribution to the AHE as the intrinsic one, and the side jump contribution can be omitted. The calculated value of the experimental IAHC for the martensite tetragonal phase is nearly 10 times lower than that of theoretical IAHC; this discrepancy might be related to the formation of twin domains. The experimental findings show that the AHC in the low-temperature martensite phase is governed by the intrinsic mechanism to a greater extent as compared to the high-temperature phase. Notably, the theoretically calculated value of IAHC for the austenite cubic phase is smaller than the theoretical IAHC for the martensite phase, which agrees with the experimental result in some aspect that as we move from the less symmetric tetragonal phase to the highly symmetric cubic phase, the intrinsic mechanism is being suppressed. These results make one additional conclusion that there is no straightforward rule to connect the Berry curvature to the mirror symmetry; rather, it depends on the symmetry-induced change in the electronic band structure.

References

[1] S. Singh, B. Dutta, S. W. D Souza, M. G. Zavareh, P. Devi, A. S. Gibbs, T. Hickel, S. Chadov, C. Felser, and D. Pandey. Robust Bain distortion in the premartensite phase of a platinum-substituted Ni_2MnGa magnetic shape memory alloy. Nat. Commun. **8**, 1006 (2017).

[2] J. Kübler, A. R. Williams, and C. B. Sommers, Formation and coupling of magnetic moments in Heusler alloys. Phys. Rev. B **38**, 1745-1755 (1983).

[3] G. D. Liu, X. F. Dai, S. Y. Yu, Z. Y. Zhu, J. L. Chen, and G. H. Wu, Physical and electronic structure and magnetism of Mn_2NiGa: Experiment and density-functional theory calculations. Phys. Rev. B **74**, 054435 (2006).

[4] G. D. Liu, J. L. Chen, Z. H. Liu, X. F. Dai, and G. H. Wu, Martensitic transformation and shape memory effect in a ferromagnetic shape memory alloy: Mn_2NiGa. Appl. Phys. Lett. **87**, 262504 (2005).

[5] Z. Nishiyama, Martensite Transformation, Academic Press, NewYork 1978.

[6] K. Bhattacharya, Microstructure of Martensite: Why It Forms and How It Gives Rise to the Shape-Memory Effect Oxford Univ. Press, DOI (2003).

[7] K. Otsuka, C.M. Wayman, Shape memory materials, Cambridge university press 1999.

[8] K. Ullakko, Magnetically controlled shape memory alloys: A new class of actuator materials, Journal of materials Engineering and Performance, 5 (1996) 405-409.

[9] K. Ullakko, J.K. Huang, C. Kantner, R.C. O'Handley, V.V. Kokorin, Large magnetic□field□ induced strains in Ni_2MnGa single crystals, Applied Physics Letters, **69** (1996) 1966-1968.

[10] A. De, A.K. Singh, S. Singh, S. Nair, Temperature dependence of the anomalous Nernst effect in Ni_2MnGa shape memory alloy, Physical Review B, **103** (2021) L020404

[11] K. Ullakko, J. Huang, C. Kanter, V. Kokorin, R. O'Handley, Magnetic-field-induced strain in Ni_2MnGa shape-memory alloy, Journal of Applied Physics, **81** (1997) 5416-5416.

[12] A. Sozinov, A.A. Likhachev, N. Lanska, K. Ullakko, Giant magnetic-field-induced strain in NiMnGa seven-layered martensitic phase, Applied Physics Letters, **80** (2002) 1746-1748.

[13] M. Siewert, M. Gruner, A. Dannenberg, A. Chakrabarti, H. Herper, M. Wuttig, S. Barman, S. Singh, A. Al-Zubi, T. Hickel, Designing shape-memory Heusler alloys from first-principles, Applied Physics Letters, **99** (2011) 191904.

[14] S. Singh, K.R.A. Ziebeck, E. Suard, P. Rajput, S. Bhardwaj, A.M. Awasthi, S.R. Barman, Modulated structure in the martensite phase of $Ni_{1.8}Pt_{0.2}MnGa$: A neutron diffraction study, Applied Physics Letters, **101** (2012) 171904.

[15] Y. Sakuraba, K. Hyodo, A. Sakuma, and S. Mitani, Giant anomalous nernst effect in the $Co_2MnAl_{1-x}Si_x$ Heusler alloy induced by Fermi level tuning and atomic ordering, Phys. Rev. B **101**, 134407 (2020).

[16] F. Mende, J. Noky, S. N. Guin, G. H. Fecher, K. Manna, P. Adler, W. Schnelle, Y. Sun, C. Fu, and C. Felser, Large Anomalous Hall and Nernst Effects in High Curie-Temperature Iron-Based Heusler Compounds. Adv. Sci. **8**, 2100782 (2021).

[17] A. K. Singh, G. K. Shukla, and S. Singh, Intrinsic anomalous Hall conductivity and real space

Berry curvature induced topological Hall effect in Ni_2MnGa magnetic shape memory alloy. J. Phys. D: Appl. Phys. **56**, 044004 (2023).

[18] S. Singh, B. Dutta, S. W. D'Souza, M. G. Zavareh, P. Devi, A. S. Gibbs, T. Hickel, S. Chadov, C. Felser, and D. Pandey, Robust Bain distortion in the premartensite phase of a platinum-substituted Ni_2MnGa magnetic shape memory alloy. Nat Commun **8**, 1006 (2017).

[19] S. Singh, R. Rawat, S. E. Muthu, S. W. D'Souza, E. Suard, A. Senyshyn, S. Banik, P. Rajput, S. Bhardwaj, A. M. Awasthi, R. Ranjan, S. Arumugam, D. L. Schlagel, T. A. Lograsso, A. Chakrabarti, and S. R. Barman, Spin-Valve-Like Magnetoresistance in Mn_2NiGa at Room Temperature. Phys. Rev. Lett. **109**, 246601 (2012).

[20] S. Rastogi, N. Shahi, V. Kumar, G. K. Shukla, S. Bhattacharjee and S. Singh, Revealing the origin of the topological Hall effect in the centrosymmetric shape memory Heusler alloy Mn_2NiGa: A combined experimental and theoretical investigation. Phys. Rev. B (2023).

[21] P. Giannozzi, S. Baroni, N. Bonini, M. Calandra, R. Car, C. Cavazzoni, D. Ceresoli,. G. L. Chiarotti, M. Cococcioni, I. Dabo, A. D. Corso, S. de Gironcoli, S. Fabris, G. Fratesi, R. Gebauer, U. Gerstmann, C. Gougoussis,A. Kokalj, M. Lazzeri, L. Martin-Samos, N. Marzari, F. Mauri, R. Mazzarello, S. Paolini, A. Pasquarello, L. Paulatto, C. Sbraccia, S. Scandolo, G. Sclauzero, A. P.Seitsonen, A. Smogunov, P. Umari, and R. M. Wentzcovitch, QUANTUM ESPRESSO: a modular and open-source software project for quantum simulations of materials. J. Phys. Cond. Matt. **21**, 395502 (2009).

[22] J. P. Perdew, K. Burke, and M. Ernzerhof, Generalized Gradient Approximation Made Simple. Phys. Rev. Lett. **77**, 3865 (1996).

[23] D. R. Hamann, Optimized norm-conserving Vanderbilt pseudopotentials. Phys. Rev. B **88**, 085117 (2013).

[24] N. Marzari and D. Vanderbilt, Maximally localized generalized Wannier functions for composite energy bands. Phys. Rev. B **56**, 12847(1997).

[25] I. Souza, N. Marzari, and D. Vanderbilt, Maximally localized Wannier functions for entangled energy bands. Phys. Rev. B **65**, 035109 (2001).

[26] G. Pizzi, V. Vitale, R. Arita, S. Blügel, F. Freimuth, G. Géranton, M. Gibertini, D. Gresch, C. Johnson, T. Koretsune, J. I.-Azpiroz, H. Lee, J.-M. Lihm, D. Marchand, A. Marrazzo, Y. Mokrousov, J. I. Mustafa, Y. Nohara, Y. Nomura, L. Paulatto, S. Poncé, T. Ponweiser, J. Qiao, F. Thöle, S. S. Tsirkin, M. Wierzbowska, N. Marzari, D. Vanderbilt, I. Souza, A. A. Mostofi, and J. R. Yates, Wannier90 as a community code: new features and applications. J. Phys. Cond. Matt. **32**, 165902 (2020).

[27] T. Kida, L. A. Fenner, A. A. Dee, I. Terasaki, M. Hagiwara, and A. S. Wills, The giant anomalous Hall effect in the ferromagnet Fe3Sn2—a frustrated kagome metal. J. Phys.: Condens. Matter. **23** 112205 (2011).

[28] C. M. Hurd, *The Hall Effect in Metals and Alloys* (Plenum, New York, 1972).

[29] G. K. Shukla, J. Sau, N. Shahi, A. K. Singh, M. Kumar, and S. Singh, Anomalous Hall effect from gapped nodal line in the Co2FeGe Heusler compound. Phys. Rev. B **104**, 195108 (2021).

[30] A. P. Kamantsev, Yu. S. Koshkid'ko, E. O. Bykov, V. S. Kalashnikov, A. V. Koshelev, A. V. Mashirov, I. I. Musabirov, M. A. Paukov, and V. V. Sokolovskiy, Magnetocaloric and Shape Memory Effects in the Mn_2NiGa Heusler Alloy. Phys. Solid State, **62**, 815–820 (2020).

[31] N. Shahi, A. K. Jena, G. K. Shukla, V. Kumar, S. Rastogi, K. K. Dubey, I. Rajput, S. Baral, A. Lakhani, S.-C. Lee, S. Bhattacharjee, and S. Singh, Antisite disorder and Berry curvature driven anomalous Hall effect in the spin gapless semiconducting Mn_2CoAl Heusler compound. Phys. Rev. B **106**, 245137 (2022).

[32] S. Roy, R. Singha, A. Ghosh, A. Pariari, and P. Mandal, Phys. Rev. B **102**, 085147 (2020).

[33] G. K. Shukla, J. Sau, V. Kumar, M. Kumar, and S. Singh, Band splitting induced Berry flux and intrinsic anomalous Hall conductivity in the NiCoMnGa quaternary Heusler compound. Phys. Rev. B **106**, 045131 (2022).

[34] Q. Zhang, P. Li, Y. Wen, C. Zhao, J. W. Zhang, A. Manchon, W. B. Mi, Y. Peng, and X. X. Zhang, Anomalous Hall effect in Fe/Au multilayers. Phys. Rev. B **94**, 024428 (2016).

[35] N. Nagaosa, J. Sinova, S. Onoda, A. H. MacDonald, and N. P. Ong, Anomalous Hall effect. Rev. Mod. Phys. **82**, 1539 (2010).

[36] C. Zeng, Y. Yao, Q. Niu, and H. H. Weitering, Linear Magnetization Dependence of the Intrinsic Anomalous Hall Effect. Phys. Rev. Lett. **96**, 037204 (2006).

[37] S. A. Yang, H. Pan, Y. Yao, Q. Niu, Scattering universality classes of side jump in the anomalous Hall effect. Phys. Rev. B **83**, 125122 (2011).

[38] R. P. Jena, D. Kumar, and A. Lakhani, Scaling analysis of anomalous Hall resistivity in the Co_2TiAl Heusler alloy, J. Phys.: Condens. Matter **32**, 365703 (2020).

[39] P. Saha, M. Singh, V. Nagpal, P. Das, and S. Patnaik, Scaling analysis of anomalous Hall resistivity and magnetoresistance in the quasi-two-dimensional ferromagnet Fe_3GeTe_2. Phys. Rev. B **107**, 035115 (2023).

[40] R. L. Liboff, G. K. Schenter, Electron-phonon scattering contributions to metallic resistivity at 0 K. Phys. Rev. B **54**, 16591 (1996).

[41] P. V. Prakash Madduri and S. N. Kaul, Magnon-induced interband spin-flip scattering contribution to resistivity and magnetoresistance in a nanocrystalline itinerant-electron ferromagnet: Effect of crystallite size. Phys. Rev. B **95**, 184402 (2017).

[42] R. Xu, A. Husmann, T. F. Rosenbaum, M.-L. Saboungi, J. E. Enderby, and P. B. Littlewood, Large magnetoresistance in non-magnetic silver chalcogenides. Nature **390** 57-60 (1997).

[43] B. Raquet, M. Viret, E. Sondergard, O. Cespedes, and R. Mamy, Electron-magnon scattering and magnetic resistivity in 3d ferromagnets, Phys. Rev. B **66**, 024433 (2002).

[44] A. P. Mihai, J. P. Attané, A. Marty, P. Warin, and Y. Samson, Electron-magnon diffusion and magnetization reversal detection in FePt thin films, Phys. Rev. B **77**, 060401(R) (2008).

[45] P. J. Brown, T Kanomata, K. Neumann, K. U. Neumann, B. Ouladdiaf, A. Sheikh, and K. R. A. Ziebeck, Atomic and magnetic order in the shape memory alloy Mn_2NiGa. J. Phys.: Condens. Matter. **22** 506001 (2010).

[46] J. Kübler and C. Felser, Berry curvature and the anomalous Hall effect in Heusler compounds. Phys. Rev. B **85**, 012405 (2012).

[47] A. Kundu, M. E. Gruner, M. Siewert, A. Hucht, P. Entel, and S. Ghosh, Interplay of phase

sequence and electronic structure in the modulated martensites of Mn_2NiGa from first-principles calculations. Phys. Rev. B **96**, 064107 (2017).

[48] Souvik Paul, Ashis Kundu, Biplab Sanyal, and Subhradip Ghosh, Anti-site disorder and improved functionality of Mn_2NiX (X = Al, Ga, In, Sn) inverse Heusler alloys. J. Appl. Phys. **116**, 133903 (2014).

[49] G. K. Shukla, A. K. Jena, N. Shahi, K. K. Dubey, I. Rajput, S. Baral, K. Yadav, K. Mukherjee , A. Lakhani, K. Carva, S.-C. Lee, S. Bhattacharjee, and S. Singh, Atomic disorder and Berry phase driven anomalous Hall effect in a Co_2FeAl Heusler compound. Phys. Rev. B **105**, 035124 (2022).